ADVANCED ENGINEERING MATERIALS
www.aem-journal.com

Design, Additive Manufacturing, and Electromagnetic Characterization of Alumina Cellular Structures for Waveguide Antenna

*Alice Rosa, Samuel Poretti, Giacomo Milan, and Alberto Ortona**

In this work, a design and additive manufacturing approach is successfully implemented to print via digital-light-processing cubic cellular alumina structures for antenna waveguides. Cellular structures' porosity is varied during the design phase and different dielectrics are finally produced and inserted in antenna waveguides with the aim of decreasing the cutoff frequency in the range from 1 to 10 GHz. In parallel, the electromagnetic behavior of the cellular alumina structures into the antenna waveguide as the structure porosity varies is simulated. Printed samples are then tested in a laboratory setup. In the results obtained, it is shown that the antenna cutoff frequency increases as the porosity of the alumina cellular structures increases, also evidencing a linear correlation between their average dielectric constant and porosity. In this study, it is demonstrated that the dimensional accuracy achieved after the sintering process is essential because even a small (1%) deviation of the sintered sample size from the nominal ones, due to nonlinear shrinkage, highly affects their cutoff frequencies.

1. Introduction

Nowadays, additive manufacturing (AM) technologies are gaining more and more importance due to their ability to produce complex components.[1] AM techniques can be divided among the different materials families they are able to process; in this article, we will focus on ceramics because of their favorable electromagnetic properties.

Cellular ceramic structures belong to a class of hybrid materials that consist of a solid ceramic component and a hollow region that is typically gas-filled.[2] Both the solid and hollow parts of the structure contribute to its final properties. For instance, the conductivity of the gas inside the pores affects the thermal conductivity of low-density foams used as insulation. Gas properties can also affect compressibility and dielectric characteristics.[3] In contrast, the shape and size of the cells have a great influence on the properties of the final structure.[4] Many shapes can be used to build the desired structure, even combining different shapes together to achieve specific properties (**Figure 1**).

Among the available AM techniques stands digital light processing (DLP) which employs a projector as the light source implying the photopolymerization of a reactive system, called slurry, containing ceramic particles, photopolymerizable resins, and additives.[5–7] A peculiarity of the DLP technique is the ability to produce complex ceramic components because of their high resolution. This capability is needed when a porous geometry, obtained by the reproduction into the space of a unitary cell like the one in Figure 1 should be realized.

In general, regarding porous ceramics fabrication, foam replica[8] is one of the most common methods to fabricate oxide ceramic cellular structures. Using this technique, complex ceramic structures with controlled porosity can be produced.[9,10] However, obtaining a uniform green (i.e., unfired) coating on the cellular polymer structure—especially if it has sharp corners—is a crucial step in this procedure. Furthermore, if extra ceramic slurry is not completely removed during heat treatment, some closed cells may form in the finished ceramic foam, which will change its mechanical characteristics and permeability behavior.[2] Other methods to produce these types of structures are 1) gelation-freezing, 2) direct foaming of a liquid slurry, 3) burn-out of fugitive pore formers, and 4) chemical vapor deposition (CVD).[2,9,11,12] These methods show several disadvantages, among which the most important is the limited control of porosity that leads to a nonuniform cellular structure afflicting material property throughout the structure.[9]

The production of oxide cellular structures through DLP, instead, offers a wide range of advantages.[13] Indeed, DLP technology ensures high printing resolution, allowing details and porosity control and intricate features within oxide cellular structures generation. Furthermore, DLP allows for easy customization of oxide cellular structures, producing components with

A. Rosa, S. Poretti, G. Milan, A. Ortona
Department of Innovative Technologies (DTI)
University of Applied Sciences and Arts of Southern Switzerland (SUPSI)
6962 Lugano, Switzerland
E-mail: alberto.ortona@supsi.ch

A. Rosa
Department of Industrial Engineering
University of Padova
35131 Padova, Italy

The ORCID identification number(s) for the author(s) of this article can be found under https://doi.org/10.1002/adem.202302159.

DOI: 10.1002/adem.202302159

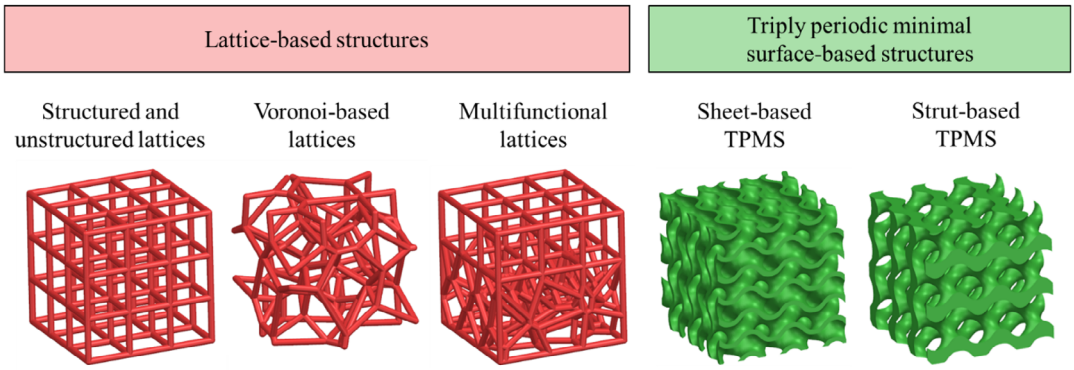

Figure 1. Different architectures of lattice structures.

specific geometries, porosities, and mechanical properties tailored to particular applications.[14–16]

The 3D-printed structures made of ceramics with favorable electromagnetic properties hold promises in the electronic field, particularly in the microwave sector.[17–19]

Indeed, standard ceramics already find various applications in the microwave sector.[20] In fact, thanks to the stable relative permittivity, otherwise known as dielectric constant (ε_r), and the low dielectric loss (tanδ),[21] they are applied as critical constituents in wireless communications systems or in general in systems operating in the microwave frequency range. These materials have typically been used for several years specifically for the development of resonators, filters, capacitors, printed circuits, and more.[22,23] Ceramic materials find applications in the antenna development, again thanks to their dielectric constant and loss factor values which respectively allow the obtaining of radiating structures (antennas) of reduced dimensions and losses[24,25] or lenses.[26,27] For all these structures, the dielectric constant represents an important variable that influences several microwave components characteristics such as the resonance frequency of antennas and resonators, the propagation speed of ceramic substrates used for printed antennas, and filters or the refraction characteristics in the case of dielectric lenses. A ceramic material of particular interest is alumina (Al_2O_3), because of its excellent dielectric, thermal, mechanical, and chemical properties. Al_2O_3 has a high dielectric constant that can vary depending on its specific formulation and on manufacturing conditions. This property is crucial for its use in electronic and microwave devices, as it is strictly correlated to electromagnetic and electrical parameters.[17] Thanks to its stable mechanical characteristics, the possibility of producing particular shapes by computational design and AM allows, for the specific application, to expand the operating frequency of antennas.

The ceramic materials, used in their "bulk" state, have fixed dielectric constant values (i.e., Al_2O_3 ε_r from 9 to 10[21,28]), which are dependent on the material at its microscopic scale. Often these values are not totally in line with the designers' needs and it is not possible to tune them. This work intends to delve into a possible approach for the production of complex ceramic structures with variable dielectric constant by combining the characteristics of ceramic materials with their ability to be 3D printed into complex structures with variable dielectric constants.[19,29] As a consequence, the challenges of this work are to obtain near to net shape complex architectures with high resolution and good integrity. This leads to optimize the shape, density, and size of the alumina cellular structure to vary the overall dielectric constant without affecting the electrical behavior at the macroscopic level.

2. Experimental Section

2.1. Antennas and Structure Description

The main goal is to analyze the possibility of progressively reducing the operating frequency of open waveguide antennas (**Figure 2**) by inserting a dielectric material (alumina cellular

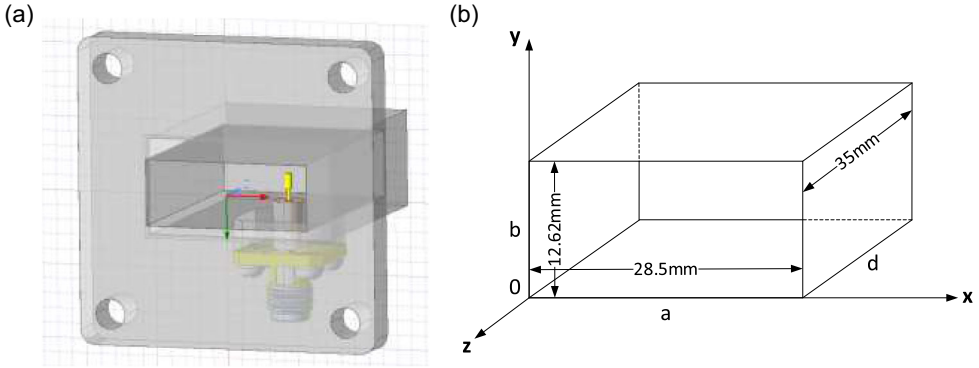

Figure 2. Waveguide adapter: a) 3D view and b) internal dimensions.

structure) inside them. For this purpose, a standard commercial size WR112 (Electronic Industries Alliance standard) or WG15 (Radio Components Standardization Committee standard) was used as a reference for the experiments. The recommended frequency band for this model was from 7.05 to 10 GHz with a cutoff frequency (non-filled lowest propagation order mode) of 5.26 GHz.

The intent was to fill the internal space with the developed material. Since the only access to the internal space of the antenna was the front window, a particular shape of filling object was designed to be inserted from that side without having contact with the active part of the antenna which is located within the space available.

2.2. Design of the Alumina Cellular Structures

As explained in ref. [30], printing by DLP technology and sintering bulk alumina cellular structures without defects such as cracks and delaminations was extremely difficult. Indeed, this technique had limits when producing ceramic components with wall thicknesses more than 10 mm. This was due to the fact that the green bodies contained a significant amount of organic binder, which evacuated from the internal microstructure during thermal debinding and caused defects formation on the surface at the interface between layers.[31] Porous structures, such as lattices, having a larger surface area and an average lower bulk thickness, better allowed the decomposed binder to evacuate from the material, thus avoiding the formation of defects in the structures.[30]

The lattice structures used in this initial study were generated by replicating a cubic unit cell in the three directions x, y, and z (Figure 2b) using the commercial software Siemens NX 1984 (Siemens, Munich, Germany). Given the small size of the cells, compared to the wavelength of the employed frequencies, cell shape dis not affect structure electromagnetic behaviors.[32] For this specific study, it was therefore decided to employ the cubic unit cell, instead of using more complex cells (Figure 1) would have required too much computational time for electromagnetic simulations. The alumina lattice structures were designed by keeping the shape, the outer dimensions and the cell type fixed, while varying the size of the windows ($0.4 \div 2.0$ mm) and the size of the struts ($0.2 \div 6.4$ mm) to change the porosity of the structure.

Figure 3 shows three representative cubic cell structures with different cells dimensions implying high, medium, and low porosity of the structure. Beveled edges were added to facilitate insertion of the object into the waveguide antenna and avoid friction. Additionally, Figure 3 provides a detailed view of a unitary cubic cell highlighting the window (W) and the strut (S).

2.3. Simulations with Ansys Electronics

The electromagnetic behavior of the structure inserted into the waveguide antenna was first estimated and analyzed using the commercial finite element electromagnetic simulator Ansys HFSS (Ansys, Canonsburg, USA). Different alumina ($\varepsilon_r = 9.6$ and $\tan\delta = 0.006$) infill patterns were simulated in terms of size and structure. Since the external part of the waveguide structure had little influence on the electromagnetic results, the model was simplified by representing only the internal part of the antenna by adding perfect conductive walls on the external edges (**Figure 4**). Boundary conditions box was set to radiation at a distance of 50 mm from each antenna side.

All analyses were carried out in a frequency range from 1 to 8 GHz by analyzing the reflection coefficient (S11 parameter) all over the investigated bandwidth. The tool used generated the mesh automatically and adaptively, based on the central analysis frequency. A central analysis frequency of 6 GHz was set in the model to obtain the desired accuracy even at the highest frequencies of the analysis range. In the realm of waveguide antennas, the S11 parameter played a pivotal role in evaluating the

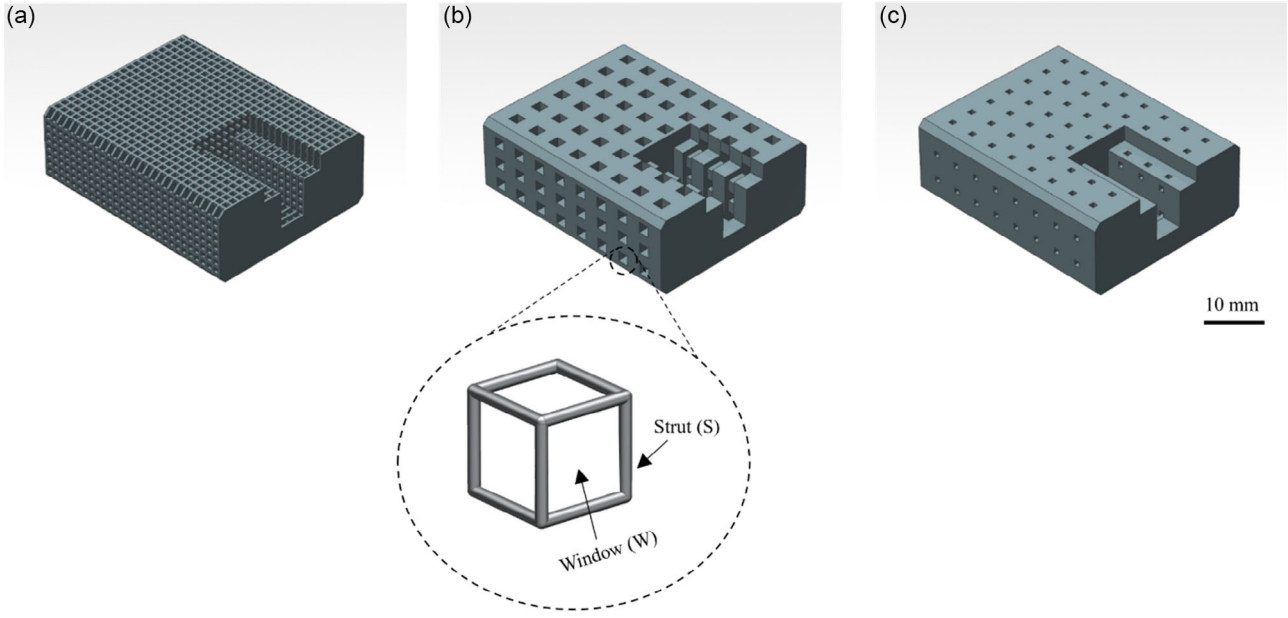

Figure 3. Cubic cell structures: a) W 1.0 mm, S 0.4 mm—porosity 58%; b) W 2.0 mm, S 2.8 mm—porosity 25%; and c) W 1.0 mm, S 3.6 mm—porosity 6%.

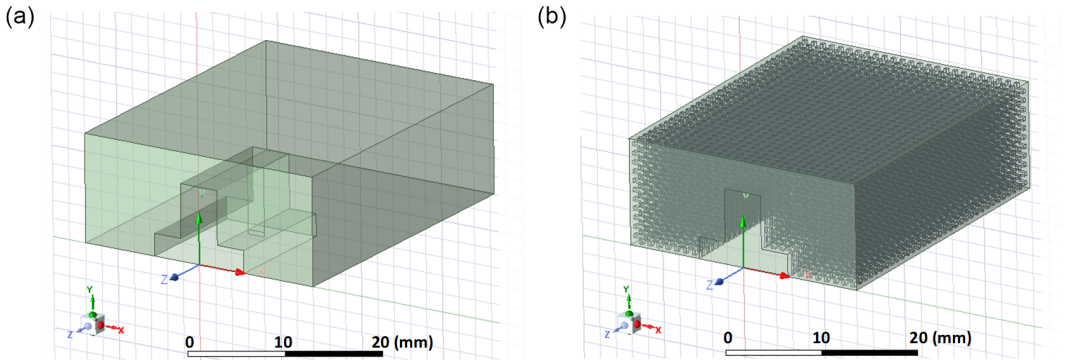

Figure 4. Simulation model: a) bulk filling material and b) porous pattern.

antenna's ability to efficiently transmit and receive electromagnetic waves. Specifically, S11 measured the reflection coefficient at the input port of the waveguide antenna. This parameter provided insights into how much of the incident electromagnetic wave was reflected back into the waveguide, influencing the overall antenna performance.

2.4. Materials

The alumina cellular structures were 3D printed employing the industrial DLP device Admaflex 130 (Admatec, NL) specifically intended to print ceramic parts starting from photocurable ceramic slurries.

The ceramic suspension was obtained by first drying α-Al_2O_3 powders (SA8MAR, Baikowski, France, specific surface area: 8.94 $m^2\,g^{-1}$, d50 = 0.31 μm) for 2 h at 150 °C in an oven under vacuum and then by dispersing them at 50 vol% in a monomer-based mixture composed of a difunctional monomer (1,6-hexanediol diacrylate, HDDA, Allnex GMBH, Germany) at 70 wt% and a tetrafunctional monomer (EBECRYL 892, Allnex GMBH, Germany) at 30 wt%. As photoinitiator, Omnirad 819 (IGM Resins B.V., Netherlands) was employed at 0.4 wt% (with respect to the monomer mixture). The dispersant used was a copolymer with a phosphoric acid ester group (DisperBYK-111, BYK-Chemie GmbH, Germany) at 2 wt% with respect to the powders and poly(ethylene glycol) diacrylate (Merck & Cie, Switzerland) was used as a diluent at 25 wt% with respect to the monomer mixture. Additionally, a yellow dye was added at 0.1 wt% (with respect to the slurry) as light absorber. A 3D mixer, Thinky Mixer ARE-250 (Thinky USA Inc., USA), was used to homogenize the constituents. The speed and duration were set at 1000 rpm and 2 min, respectively.

2.5. Thermal Treatments

Thermal treatments were performed in air using the muffle furnace L40-11 BO (Nabertherm GmbH, Germany) for the debinding phase and the muffle furnace LHT-08-18 (Nabertherm GmbH, Germany), for the sintering phase.

To define a proper thermal debinding for the developed formulation, a thermo gravimetric analysis/digital scanning calorimetry (TGA/DSC) analysis on a cylindrical sample (d 6 mm, h 6 mm) achieving a temperature of 800 °C with a heating rate of 5 °C min^{-1} was performed. **Figure 5** shows the resulting graphs of TGA and DSC.

Starting from the TGA/DSC analysis, the thermal cycle was designed with a long debinding stage lasting about 48 h. The debinding temperature range (from ambient temperature

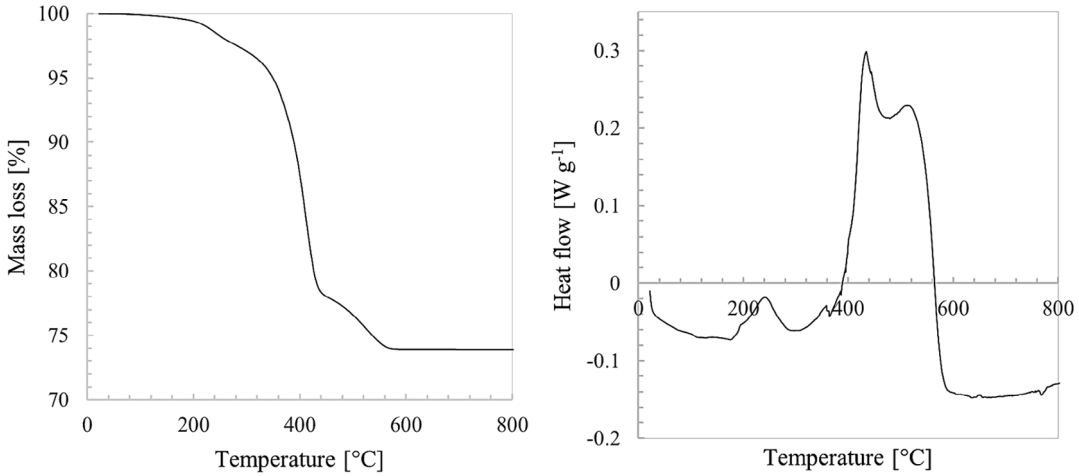

Figure 5. TGA and DSC analyses on samples printed with the formulation described in Section 2.4, "Materials".

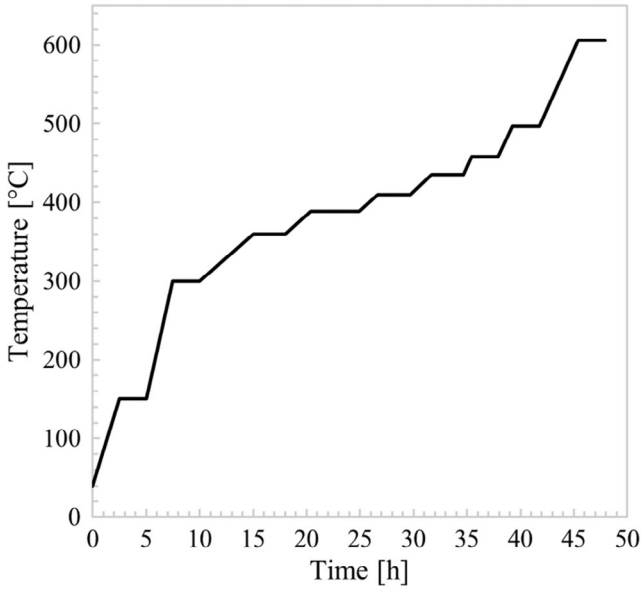

Figure 6. Debinding profile designed from TGA/DSC analyses.

to roughly 600 °C) included many isothermal intervals. This strategy allowed for temperature uniformity and the reduction of temperature gradients between the component's external and internal surfaces. The heating rate from ambient temperature up to 300 °C was set to 1 °C min^{-1} and 2 h 30 min dwell was added at 150 °C. From 300 to 410 °C, the heating rate was 0.2 °C, and from 435 to 606 °C the heating rate was 0.5 °C. In this temperature range, dwells of 4 h 30 min and 2 h 30 min were added at the most critical temperatures. **Figure 6** shows the designed debinding profile.

Concerning the sintering phase, the heating rate to reach the sintering temperature was set to 1 °C min^{-1} and some dwells of 2 h 30 min were added before the sintering temperature to homogenize the samples temperature. The sintering phase temperature corresponded to 1625 °C with a dwell of 2 h.

2.6. Characterization

2.6.1. Density

The density of the samples was determined by the double-weight method, employing the precision balance PLJ 600-3CM (Kern, Germany) coupled with the density measurement apparatus PLS-A01 (Kern, Germany). The samples used were cylinders of Ø 10.00 mm and h 10.00 mm. The procedure was based on the Archimedes principle. The Al_2O_3 theoretical density of 3.94 g cm^{-3} was used as reference value to calculate the relative density of the alumina 3D-printed samples.

2.6.2. Stereomicroscope

To perform morphological evaluations (i.e., breaking surface, cracks, etc.), the stereomicroscope Stemi 2000C (Zeiss, Germany) equipped with a digital camera for image acquisition was employed.

The samples were inspected on the face where the layers can be distinguished with respect to the direction of observation.

2.6.3. Electromagnetic Lab Test Setup

Laboratory tests were conducted using commercial antenna models and measured using the Keysight (Agilent) N5230A Vector Network Analyzer (VNA) (Testwall GmbH, Berlin, Germany) in the 1–8 GHz frequency band. To obtain a direct comparison with the simulation results, the reflection coefficient S11 was taken into consideration in this case too.

In addition to the direct analysis of the S11 parameter to identify the cutoff frequency of the antenna, the average dielectric constant of the interior of the antenna was estimated, both for the simulations and for the laboratory measurements. Given the waveguide structure represented in **Figure 7**, Equation (1) shows the waveguide cutoff frequency for the different propagation modes m and n, where c is the speed of light in vacuum.

$$f_{c_{mn}} = \frac{c}{2\pi\sqrt{\mu\varepsilon}} \cdot \sqrt{\left(\frac{m\pi}{a}\right)^2 + \left(\frac{n\pi}{b}\right)^2} \tag{1}$$

The lowest cut-off frequency was obtained for the so-called dominant mode, which for rectangular waveguides was the TE_{10} mode with $m = 1$ and $n = 0$. As regards the material under examination, we could simplify the permeability contribution by assuming a value equal to 1 therefore resulting in the following simplified equation:

$$f_{c_{10}} = \frac{c}{2a\sqrt{\varepsilon}} \tag{2}$$

The calculation of the mean permittivity or dielectric constant could therefore be represented as in Equation (3) starting from Equation (2).

$$\varepsilon = \left(\frac{c}{2af_c}\right)^2 \tag{3}$$

The estimate of the average dielectric constant of the structure inserted in the guide could therefore be obtained starting from the lower cutoff frequency obtained from the frequency analysis of parameter S11 (**Figure 8**). Since the amplitude of the first resonance was variable during the tests, the minimum value of the

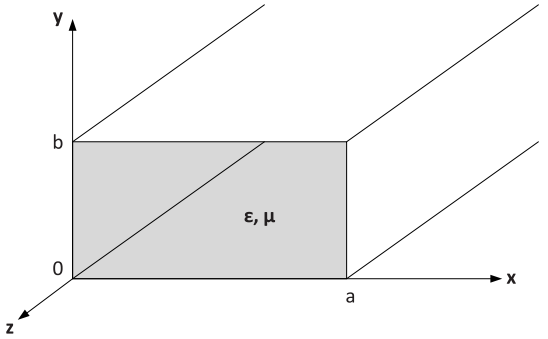

Figure 7. Waveguide structure filled with a material with permittivity ε and permeability μ.

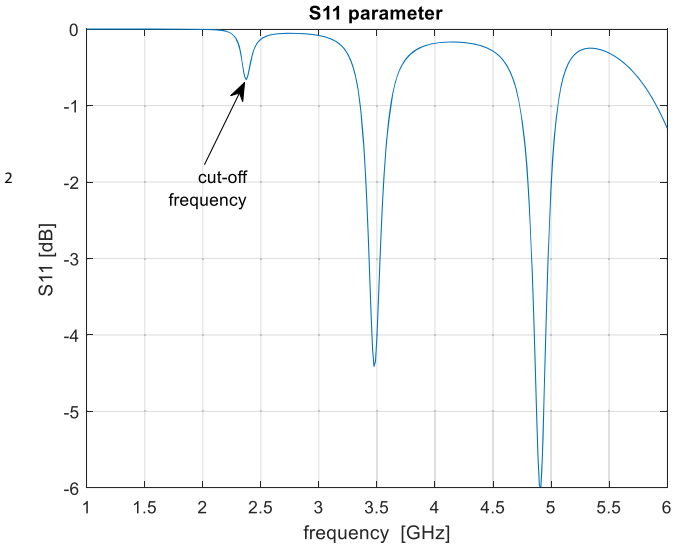

Figure 8. Example of simulated S11 parameter.

first resonance peak was taken as reference to determine its relative frequency.

3. Results and Discussion

3.1. Material Properties and Integrity

The density measurements on the 3D-printed and sintered material using the Archimedes' method gave measured values of 3.82 g cm^{-3} and 97% of the theoretical density of alumina (3.94 g cm^{-3}). The volumetric shrinkage of the sintered material with respect to the green one is around 19%. These two properties of the sintered material suggest that the thermal debinding and sintering cycle used resulted in good densification of the alumina components produced by DLP technique.

Figure 9 shows a representative sample of a) a green and b) sintered alumina cellular structure with cubic cell (W 1.0 mm, S 0.8 mm, and porosity 42%).

The developed material allows the production by DLP technique of alumina cellular structures with different porosities, which, as explained in the next paragraphs, enables the dielectric constant value to be modulated according to requirements. **Figure 10** shows several stereomicroscope images of sintered alumina cellular structures with different porosities and struts sizes.

What emerges is that structures with thick struts (S 1.6 mm) show much more delaminations than structures with thin struts (S 0.2 mm), which instead have a more homogeneous structure. The reason of the increased occurrence of defects and delaminations after sintering is that thicker components have more ceramic powder present in their microstructures, which causes the decomposed species' path out of the structure during the debinding phase to be very tortuous.[31] The interface between each layer is the most critical region of a part that is 3D printed. There is a continuity solution at each layer's interface since the DLP technology produces 3D objects by stacking 2D layers on top of each other. Cracks and delaminations between layers may

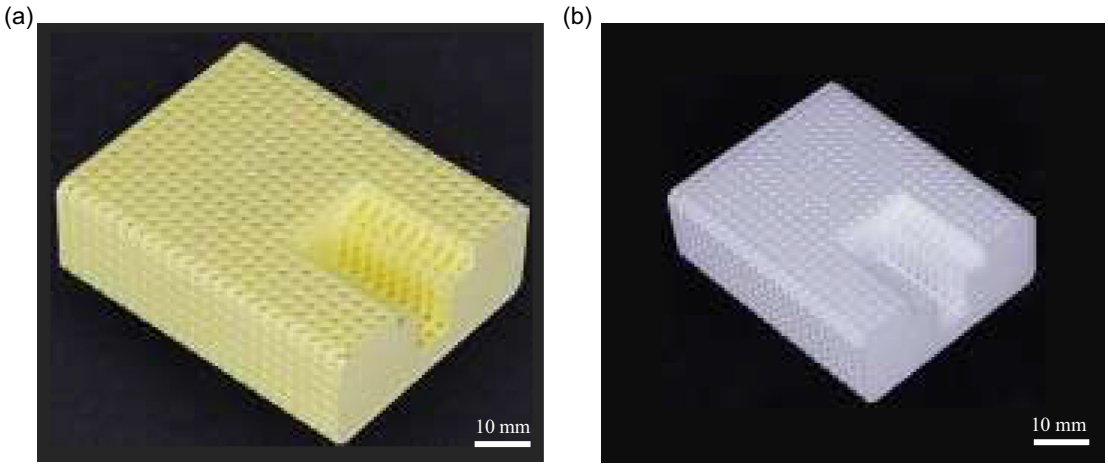

Figure 9. a) As-printed "green" and b) as-sintered representative alumina cubic cell structures (W 1.0 mm, S 0.8 mm—porosity 42.3%).

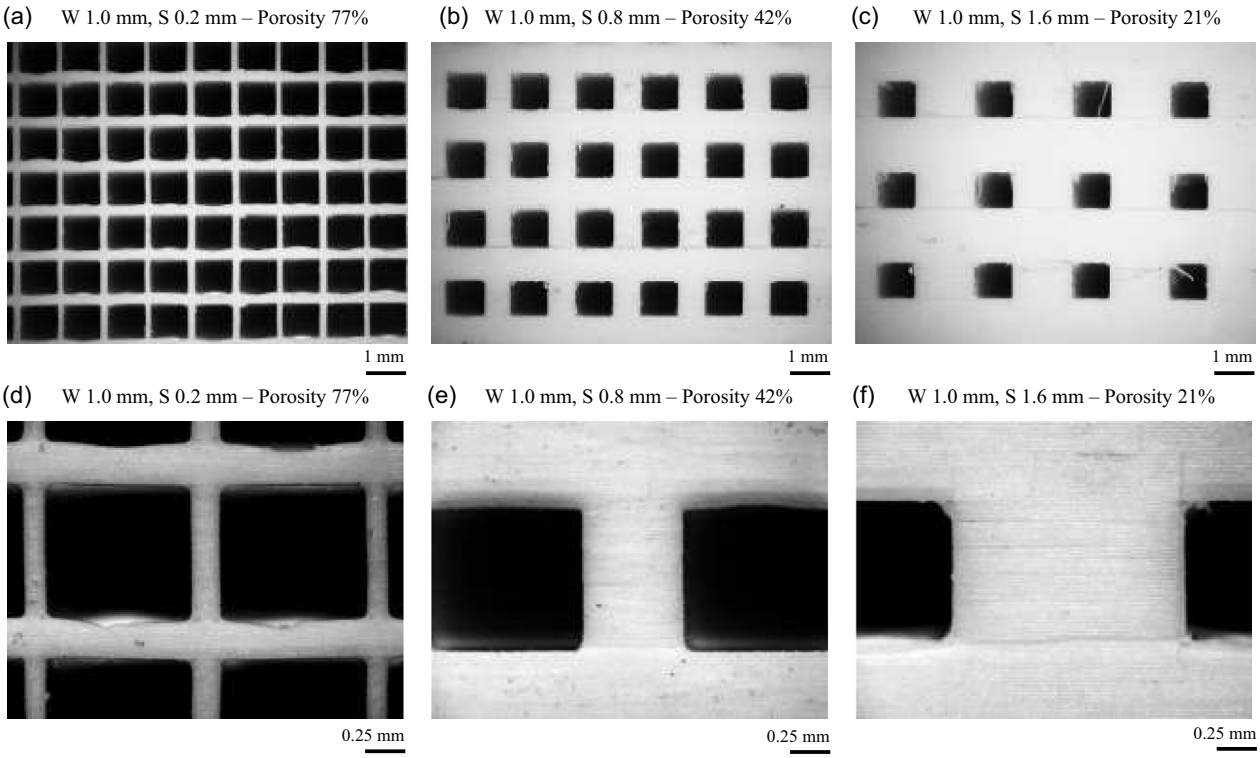

Figure 10. Stereo-microscope images of alumina cellular structures with different porosities: a,d) W 1.0 mm, S 0.2 mm—porosity 77%; b,e) W 1.0 mm, S 0.8 mm—porosity 42%; and c,f) W 1.0 mm, S 1.6 mm—porosity 21%.

result from this interface during the thermal treatment due to the evacuation of the decomposition products.[30] In contrast, alumina cellular structures with higher porosity, particularly those with strut 0.2 mm, show a nonoptimal adhesion between layers where there is a change in cross section, particularly at the end of cell windows. This is due to a nonoptimal cell size–strut size ratio, as overhangs of too large dimensions in DLP printing processes are not easily printable, except by using supports.[33]

Nevertheless, the size of these defects in Figure 10 does not affect the electromagnetic signal's microscopic behavior. This assumption is explained in the following section.

3.2. Relationship between Macroporosity, Cutoff Frequency, and Dielectric Constant

Several digital models with different macroporosity and cell dimensional characteristics were designed to be inserted in the waveguide antenna simulation model. The first determining aspect that was analyzed is that of the dimensions of the empty volumes which determine the overall porosity of the material. Since the main interest is to obtain an average dielectric constant, the structure must present a macroscopic behavior to the electromagnetic field to which it is subjected, avoiding other phenomena of resonance, scattering, etc. Of particular importance is therefore the size of the empty spaces in relation to the wavelength of the electromagnetic signal. In the specific case, considering the worst case and therefore a frequency of 8 GHz, it is possible to calculate a wavelength (Equation (4)) equal to 37.5 mm in air and 11.85 mm in bulk alumina.

$$\lambda = \frac{c}{\sqrt{\varepsilon} \cdot f} \tag{4}$$

The tests were carried out considering windows of the cellular structure, approximately 0.41, 0.83, and 1.67 mm which correspond to approximately one-tenth of the wavelength in bulk alumina. The graph in **Figure 11** shows that the behavior curves at different window sizes overlap and it is therefore possible to assume that the window sizes considered do not influence the

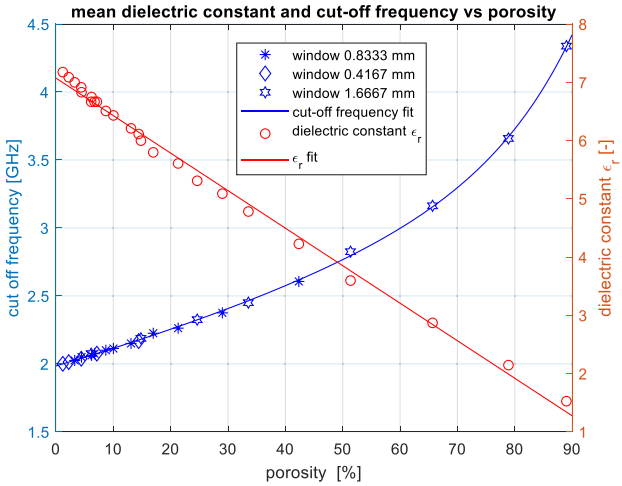

Figure 11. Simulated cutoff frequency and mean dielectric constant versus porosity for different window sizes.

Table 1. Fitting parameters for cutoff frequency estimation from porosity.

Parameter	Value
A	1.983
B	0.006293
C	0.001312
D	0.07289

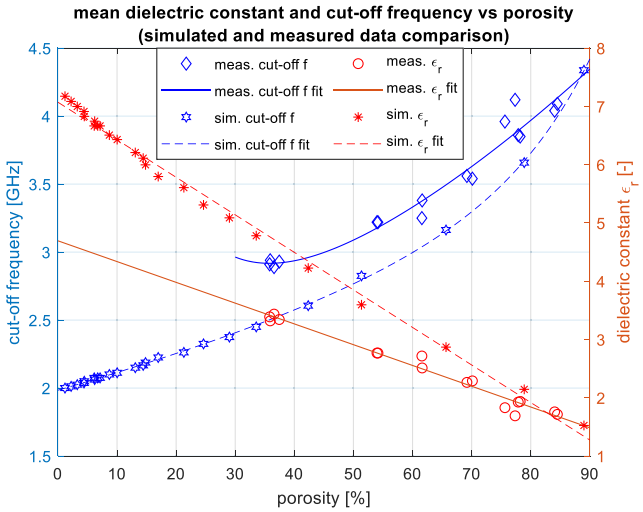

Figure 12. Cutoff frequency and mean dielectric constant versus porosity of lab samples and simulated models.

microscopic behavior of the electromagnetic signal, presenting an average dielectric constant that does not depend, in the considered range, on the size of the void pores.

The same results were therefore used to analyze the relationship between porosity and cutoff frequency of the antenna in the presence of the alumina insert with variable macroporosity. In Figure 11, it is possible to notice an exponential correlation between these two quantities.

By fitting the points with the curve expressed in Equation (5), the parameters shown in **Table 1** are obtained which can be used to estimate the cutoff frequency of the antenna as a function of the porosity of the inserted object.

$$y = a \cdot e^{b \cdot x} + c \cdot e^{d \cdot x} \tag{5}$$

The cutoff frequency is directly related to the average dielectric constant of the object inserted into the guide. Figure 11 shows the correlation between porosity and average dielectric constant obtained from the Equation (3). Estimated value at zero porosity does not reach the dielectric constant value of the material used in the simulations (9.4) as there is a part of air adjacent to the antenna in the model to allow, in subsequent laboratory measurements, the insertion of the filler object.

3.3. Lab Measurements Results and Comparisons

The simulated object models were produced through the processes described earlier and analyzed in the laboratory through the measurement setup described in Section 2.6 "Characterization". **Figure 12** shows the cutoff frequency and the average dielectric constant respectively as a function of

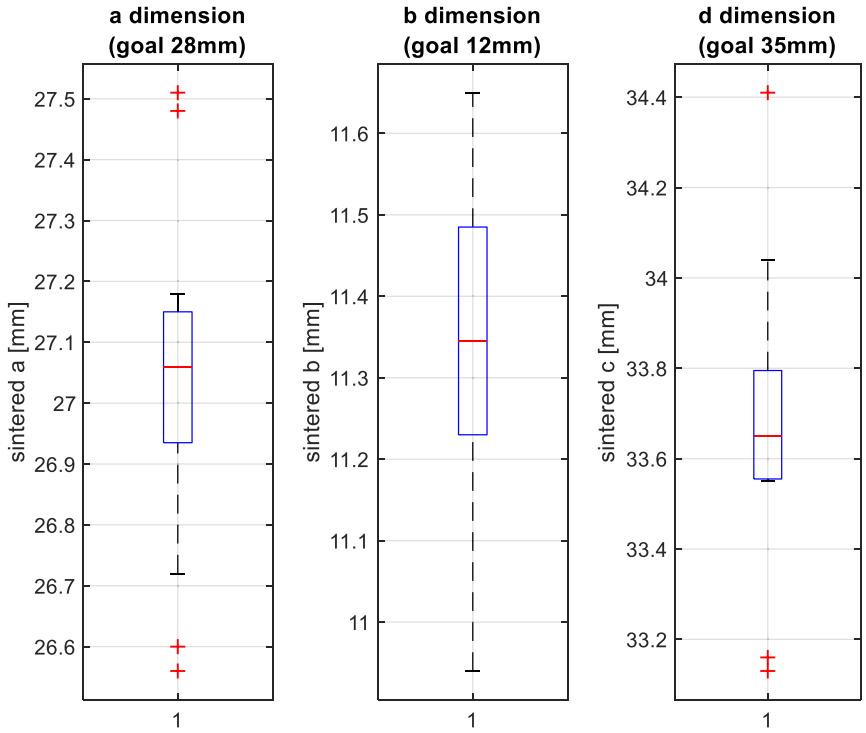

Figure 13. Physical dimensions of sintered samples variation.

Table 2. Mean dielectric constant estimation for reduced samples dimension.

Sample	Cutoff frequency [GHz]	Estimated mean dielectric constant based on Equation (3)
Bulk material with antenna gap	2.0175	7.5
Bulk material with antenna gap and reduced size of 3.6%	2.43	4.86

porosity for both simulated and measured data. Measured data curves were obtained through the same procedure adopted on the results of electromagnetic simulations.

Despite the verified trend of decreasing cutoff frequency with decreasing porosity as well as the linearity of correlation between the average dielectric constant and porosity, the two results are discordant with each other.

The parts produced after sintering have been analyzed in terms of structure and physical dimensions to evaluate the effect of the process. **Figure 13** shows the variation in the dimensions of the samples produced after the sintering process in relation to the expected dimensions used for the simulated models (Figure 2). It is possible to notice a variation compared to the expected value, albeit the maximum order of ≈1 mm. This dimensional variation is due to different shrinkage of the cubic cell alumina structures compared to the bulk cylindrical specimens used for dimensional shrinkage tests. The large thickness of bulk samples causes a temperature difference between the surface and the inside of the sample, not allowing uniform shrinkage during the sintering process. A lattice structure, in contrast, is composed of thinner struts, allowing more uniform heat distribution and, as a result, even and thus higher shrinkage than a bulk structure.[30,34] Moreover, as explained earlier, bulk specimens are more prone to have delaminations and defects already in the green component causing nonuniform sample shrinkage during the sintering process. Dielectrics, in contrast, are lattice structures composed of thin struts that do not show significant delaminations, resulting in higher shrinkage during sintering. This behavior is clearly visible in Figure 10, where alumina cellular structures with smaller struts (i.e., S 0.2 mm) have far fewer delaminations than cellular structures with larger struts (i.e., S 1.6 mm). To obtain alumina cellular structures with optimized dimensional accuracy, it is necessary to perform dedicated sintering tests for each geometry. As further development, in respect of the nonuniform shrinkage, each CAD file should be scaled accordingly.

Further electromagnetic simulations have been carried out to verify the influence caused by the reduction in sample size.

Table 2 Some representative results of the carried-out analysis. It is possible to note that for an average reduction of 3.6% of the expected dimensions, an average dielectric constant of ≈4.8 is estimated which is in line with the results obtained from the experimental tests for 0% porosity.

4. Conclusions

This study demonstrates the possibility of decreasing the cutoff frequency of waveguide antennas by means of 3D-printed alumina cellular structures. A process was developed to print, via the DLP technique, alumina cellular structures with cubic cells characterized by an average dielectric constant that can be modulated as needed by varying the porosity of the structure.

The procedure of inserting alumina cellular structures with variable porosity in waveguide antennas has demonstrated its effectiveness, allowing to obtain alumina samples with a variable average dielectric constant depending on porosity both in the field of antenna development and in general terms in the microwave field. The relationship between porosity and average dielectric constant can be further applied to materials different from alumina used in the present study. The study also highlights that in the specific case the dimensional accuracy obtained after the sintering process is of particular importance. This parameter could in any case be less influential for other applications.

Acknowledgements

Alberto Ortona personally thanks Nahum Travitzky for the passionate and inspiring conversation he had with him over the years on advanced ceramics.

Open access funding provided by Scuola universitaria professionale della Svizzera italiana.

Conflict of Interest

The authors declare no conflict of interest.

Data Availability Statement

The data that support the findings of this study are available from the corresponding author upon reasonable request.

Keywords

Al_2O_3, digital light processings, electromagnetic behaviors, electromagnetic simulations, microwaves, variable dielectric materials, waveguide antennas

Received: December 15, 2023
Revised: March 6, 2024
Published online:

[1] T. J. Horn, O. L. A. Harrysson, *Sci. Prog.* **2012**, *95*, 255.
[2] G. Bianchi, S. Gianella, A. Ortona, *J. Ceram. Sci. Technol.* **2017**, *8*, 59.
[3] M. Ashby, *J. Am. Ceram. Soc.* **2011**, *94*, S3.
[4] X. Zhang, K. Zhang, L. Zhang, W. Wang, Y. Li, R. He, *Mater. Des.* **2022**, *215*, 110470.
[5] S. Bose, N. Sarkar, S. Vahabzadeh, D. Ke, A. Bandyopadhyay, *Additive Manufacturing*, CRC Press, Boca Raton, FL **2019**, p. 183.
[6] S. Mamatha, P. Biswas, R. Johnson, *Prog. Addit. Manuf.* **2023**, *8*, 1083.
[7] R. Chaudhary, P. Fabbri, E. Leoni, F. Mazzanti, R. Akbari, C. Antonini, *Prog. Addit. Manuf.* **2023**, *8*, 331.
[8] K. Schwartzwalder, A. Somers (GEN MOTORS CORP), US3090094A, **1963**.
[9] P. Colombo, *Philos. Trans. R. Soc. A* **2006**, *364*, 109.
[10] A. Ortona, C. D'Angelo, S. Gianella, D. Gaia, *Mater. Lett.* **2012**, *80*, 95.
[11] T. Ohji, M. Fukushima, *Int. Mater. Rev.* **2012**, *57*, 115.

[12] M. Pelanconi, G. Bianchi, O. Santoliquido, F. Camerota, A. Di Mauro, A. Rosa, S. Vitullo, S. Bottacin, A. Ortona, *Additive Manufacturing*, Springer, Cham **2023**, p. 597.
[13] A. Nazir, K. M. Abate, A. Kumar, J. Y. Jeng, *Int. J. Adv. Manuf. Technol.* **2019**, *104*, 3489.
[14] J. Guo, Y. Zeng, P. Li, J. Chen, *Ceram. Int.* **2019**, *45*, 21048.
[15] Y. Liu, Z. Chen, J. Li, B. Gong, L. Wang, C. Lao, P. Wang, C. Liu, Y. Feng, X. Wang, *Addit. Manuf.* **2020**, *35*, 101348.
[16] J. S. Martinez, S. Peterson, C. A. Hoel, D. J. Erno, T. Murray, L. Boyd, J. H. Her, N. McLean, R. Davis, F. Ginty, S. J. Duclos, B. M. Davis, G. Parthasarathy, *PLoS One* **2022**, *17*, e0272283.
[17] R. Dumene, G. Earle, C. Williams, *IEEE Trans. Dielectr. Electr. Insul.* **2018**, *25*, 2236.
[18] L. Robins, A. Arsanjani, C. Bartlett, R. Teschl, W. Bosch, M. Hoft, in *2021 IEEE MTT-S Inter. Microwave Filter Workshop, IMFW 2021*, IEEE, Piscataway, NJ **2021**.
[19] S. Zhou, G. Zhang, Z. Nie, H. Liu, H. Yu, Y. Liu, K. Bi, W. Geng, H. Duan, X. Chou, *Mater. Chem. Front.* **2022**, *6*, 1736.
[20] S. B. Narang, S. Bahel, *J. Ceram. Process. Res.* **2010**, *11*, 316.
[21] A. Stiegelschmitt, A. Roosen, C. Ziegler, S. Martius, L. P. Schmidt, *J. Eur. Ceram. Soc.* **2004**, *24*, 1463.
[22] K. Wakino, *Ferroelectrics* **1989**, *91*, 69.
[23] H. Tamura, *MWE '99 Microwave Workshop Digest*, Yokohama, Japan **1999**, p. 175.
[24] B. Atabay, G. Dural, in *2019 5th Inter. Electromagnetic Compatibility Conf.*, EMC Turkiye, **2019**.
[25] Y. Wang, X. Zhang, R. Su, M. Chen, C. Shen, H. Xu, R. He, *Chin. J. Mech. Eng.: Addit. Manuf. Front.* **2023**, *2*, 100065.
[26] N. T. Nguyen, N. Delhote, M. Ettorre, D. Baillargeat, L. Le Coq, R. Sauleau, *IEEE Trans. Antennas Propag.* **2010**, *58*, 2757.
[27] Y. Wang, R. Su, J. Chen, W. Wang, X. Zhang, H. Xu, R. He, *Ceram. Int.* **2024**, *50*, 13166.
[28] R. Vila, M. González, J. Mollá, A. Ibarra, *J. Nucl. Mater.* **1998**, *253*, 141.
[29] G. Zhang, H. Wang, W. Xie, S. Zhou, Z. Nie, G. Niwamanya, Z. Zhao, H. Duan, *J. Mater. Chem. A* **2024**, *12*, 5581.
[30] O. Santoliquido, F. Camerota, A. Ortona, *Open Ceram.* **2021**, *5*, 100089.
[31] J. A. Lewis, *Annu. Rev. Mater. Sci.* **1997**, *27*, 147.
[32] X. Da Liu, Z. L. Hou, B. X. Zhang, K. T. Zhan, P. He, K. L. Zhang, W. L. Song, *Appl. Phys. Lett.* **2016**, *108*, 102902.
[33] V. Truxova, J. Safka, M. Seidl, I. Kovalenko, L. Volesky, M. Ackermann, *MM Sci. J.* **2020**, *108*, 102902.
[34] D. Karalekas, D. Rapti, E. E. Gdoutos, A. Aggelopoulos, *Exp. Mech.* **2002**, *42*, 439.